New Experimental and Modelling Approach for the Quantification of Internal Filtration

Article · May 2005

DOI: 10.2118/94634-MS

4 authors, including:

A. C. Alvarez
Instituto Nacional de Matemática Pura e Apli…
33 PUBLICATIONS **89** CITATIONS
SEE PROFILE

R. Farajzadeh
Delft University of Technology
114 PUBLICATIONS **1,054** CITATIONS
SEE PROFILE

SPE 94634

New Experimental and Modelling Approach for the Quantification of Internal Filtration

F.A.H. Al-Abduwani, SPE, Delft U. of Technology; G. Hime and A. Alvarez, Instituto Nacional de Matemática Pura e Aplicada; and R. Farajzadeh, Delft U. of Technology and Natl. Iranian Oil Co.

This paper was prepared for presentation at the SPE European Formation Damage Conference held in Scheveningen, The Netherlands, 25-27 May 2005.

1 Abstract

A new experimental methodology using X-ray Computed Tomography for studying the filtration phenomenon that occurs during the injection of water with solid particles into porous media is presented. Previously unattainable deposition profiles are used to test for conformance the widely accepted classical deep-bed filtration model, proposed by Iwasaki in 1937. An equivalent system of linear ODEs is obtained using the method of characteristics and is used in the presented analysis. Results indicate that deposition profile measurements are more valuable than typically measured effluent concentration profiles. Furthermore, it is concluded from the presented analysis that the classical model is a valid approximation to the filtration phenomenon. However, clear discrepancies between model predictions and experimental results are observed. These discrepancies could be attributed to either the kinetics equation of the classical model or the extrapolation needed to compensate for data lost due to noise. Finally, a set of recommendations for improved experiments is suggested.

2 Introduction

Water injection, whether it be sea water injection (SWI) or produced water re-injection (PWRI), is commonly used for the purposes of secondary recovery. PWRI is furthermore used for waste water management[1-7]. Yet all injection schemes suffer to varying degrees of injectivity decline, primarily depending on the injected water quality, in situ reservoir fluids and reservoir characterisation around the well.

In order to simulate the extent of injectivity decline inflicted by the injected suspensions, it is necessary to utilise a coupled model based on a transport model predicting the deposition of the impurities within the porous medium (e.g. classical deep-bed filtration[8, 9]) and a model correlating the deposition to the change in permeability it induces (i.e. the formation damage model[10, 11]).

A description of the classical deep-bed filtration model (CDBFM) will be presented in the subsequent section. It will become evident that the primary variables of the model for a suspension of solid particles are the concentration of suspended particles $\tilde{c}$, the concentration of deposited particles $\tilde{\sigma}$, and the superficial (Darcy) permeate injection velocity u_p.

Typically, the injection velocity and inlet suspension concentration of the injected fluid are kept constant in experiments. The parameters normally measured are the pressure drops over different segments of the porous medium and the effluent concentration. The latter is useful for solving the inverse problem[12-14] based on the CDBFM, which is ill-posed. The former has not been utilised to this end unless severe assumptions are made. An example is the 3-point-method[15, 16], which uses pressure values from three points along the core. It assumes a constant filtration function (i.e. a coefficient) and a specific form (linear[15] or quadratic[16]) for the formation damage model. Newly developed algorithms by Alvarez *et. al.*[17] utilise both the pressure drop and effluent concentration data to extract the filtration and formation damage function coefficients. Analyses using synthetic data with artificial noise using the above mentioned algorithms were extremely successful, while analyses utilising real data fail to produce satisfactory results[18, 19].

Thus, it becomes clear that experimental measurements of the suspended and deposited concentrations, at different times and at different locations along the porous medium, provide much more information for solving the inverse problems of the CDBFM. Kau and Lawler[20] conducted experiments using sand columns from which they measured the suspension concentration at discrete locations along the column at different times. Such a procedure is invasive and inapplicable to consolidated sandstones. Al-Abduwani *et. al.*[16, 21] developed a technique to quantify the post mortem deposition profile along a consolidated sandstone. This technique captures the deposition profile at the final time with low spatial resolution and is destructive and laborious. However, it proves the potential usefulness of measuring deposition profiles[19]. Recent advances in CT scanning technologies have allowed for higher spatial resolutions and signal sensitivity, thus enabling the measurement of the deposition profile along a porous medium at multiple locations and times[22].

This article will first describe the experimental procedure followed to obtain the deposition profile along a Bentheim sandstone using a 3rd generation CT scanner. Then multiple filtration functions that fit the experimental data are presented, and comparisons between model predictions and experimental observations for the secondary parameter (the effluent concentration) are made. Conclusions based on the comparison will be made and recommendations to the described procedures will be outlined.

3 Modelling: Deep-bed filtration model

The classical deep-bed filtration model was introduced by Iwasaki[8, 9] in 1937 and consisted of the following equations:

$$\phi\frac{\partial\tilde{c}}{\partial t}+u_p\frac{\partial\tilde{c}}{\partial x}+\frac{\partial\tilde{\sigma}}{\partial t}=0 \tag{1}$$

$$\frac{\partial\tilde{\sigma}}{\partial t}=\tilde{\lambda}(\tilde{\sigma})u_p\tilde{c} \tag{2}$$

where ϕ is the porosity; $\tilde{c}$ is the volumetric concentration of suspended particles with respect to the pore volume; $\tilde{\sigma}$ is the volumetric concentration of the deposited particles with respect to the control volume; x is the coordinate in the direction of the flow in this spatially one-dimensional problem; t is time; $\tilde{\lambda}$ is the filtration function described subsequently; and u_p is the superficial (Darcy) permeate velocity.

Equation (1) is a simplification of the convection-dispersion-reaction (CDR) equation[23, 24]:

$$\frac{\partial}{\partial t}(\phi\tilde{c}+\tilde{\sigma})+\frac{\partial Q}{\partial x}=0 \tag{3}$$

where Q is the flux of particles given by

$$Q=u_p\tilde{c}-\phi D\frac{\partial\tilde{c}}{\partial x}. \tag{4}$$

Here D is the hydrodynamic dispersion coefficient that depends on both the effective molecular diffusion coefficient and the longitudinal dispersivity of the medium[24]. The assumptions required to obtain the simplification (1) from (3) are:

1. the hydrodynamic dispersion is negligible, i.e. $D=0$;
2. the changes in porosity are negligible, i.e. $\phi\approx const$;
3. the solute and suspended particles are both incompressible;
4. the volume within the porous medium is conserved during the deposition process.

Equation (2) is a heuristic kinetics equation[8]. It assumes that the rate of particle deposition is directly proportional to the number of particles available for capture by the porous medium, namely the product of the local suspension concentration, the superficial velocity and a proportionality function $\tilde{\lambda}$ (called the *filtration function*) that has the dimensions of inverse length. The filtration function describes the deposition intensity of the suspended particles and is assumed to depend on previous deposition σ only, which is a restrictive assumption. Examples of the different forms of the filtration function hypothesised by various researchers can be seen in published reviews[9, 25].

Equations (1) and (2) are nondimensionalised using the following transformations:

$$\begin{aligned} X&=\frac{x}{L}, \quad T=\frac{u_p}{\phi L}t, \quad c=\tilde{c},\\ \sigma&=\frac{\tilde{\sigma}}{\phi}, \quad \lambda(\sigma)=L\cdot\tilde{\lambda}(\tilde{\sigma}) \end{aligned} \tag{5}$$

where L is the length of the core; the dimensionless position X lies in the interval $[0,1]$; and one unit of T is the time it takes to inject one pore volume (PVI). Dimensionless deposition σ and suspension concentration c lie in the range $[0,1]$.

Following the same derivations utilised in the inverse solution[14], we obtain the ODE on the characteristic line $(X=0)$ which governs the deposition at the injection face

$$\frac{d\sigma(0,T)}{dT}=c_i(T)\cdot\lambda(\sigma(0,T)), \tag{6}$$

and the family of ODEs on characteristic lines $(X,T+X)$ in the (X,T) plane that govern the deposition in the core:

$$\frac{d\sigma}{dX}=-\sigma\lambda(\sigma) \qquad (T>X) \tag{7}$$

where $\frac{d}{dX}$ denotes differentiation along characteristic lines $X-T=const$, i.e. $\frac{d}{dX}=\frac{\partial}{\partial X}+\frac{\partial}{\partial T}$; c_i is the dimensionless *effective* inlet concentration which varies with time; i.e. $c_i(T)=c(0,T)$. Although the inlet concentration in each experiment was kept constant, it is assumed that, due to the formation of a concentration polarization zone[26] and/or an external filter cake[27], the effective inlet concentration at the porous medium face is an unknown variable. The presented analysis of conducted experiments appears to confirm this hypothesis.

This differs from previous analyses[16, 18], where the effective inlet concentration was assumed constant. Thus, the previously developed inverse model needs to be generalised to allow for a non-constant injection concentration. Optimisation will be used to obtain the best parameters for the effective inlet concentration and filtration functions, as to best match the experimentally measured deposition profiles described in the next section. The parametric form of the effective injected concentration will be presented in the data processing section, as it was chosen based on results of intermediate data analysis. It was previously established from similar experiments[16, 18] that the filtration function was monotonically decreasing. Thus, the following three forms of filtration function were chosen for analysis (constant, linear, exponential):

$$\begin{aligned} &\lambda(\sigma)=\lambda_0 && \lambda_0>0\\ &\lambda(\sigma)=\lambda_0(1-a\sigma) && 0<a<1\\ &\lambda(\sigma)=\lambda_0 e^{-\alpha\sigma} && \lambda_0>0,\alpha>0 \end{aligned} \tag{8}$$

Comparative results will be presented in §6 of this article.

4 Experimental study

The primary objective of the developed crossflow setup (schematic depicted in Figure 1) was to measure the following parameters:

1. the deposition profiles within the porous medium;
2. the effluent concentration, using the CT scanner (SAMATOM Volume Zoom quad-slice manufactured by Siemens) and using other techniques;
3. the pressure drop over multiple segments of the core;

4. the thickness of the external cake, using the CT scanner and using other techniques;
5. the pressure drop over the external filter cake.

This article is concerned with the deep-bed filtration related objectives, primarily 1 and 2. The external filter cake objectives are treated in a separate publication[27].

The crossflow filtration unit (CFFU) was constructed from polyether ether kentone (PEEK), as it has a low value of local linear attenuation coefficient μ when compared to other construction materials such as stainless steel[28]. Two outer aluminium flanges were incorporated along with eight bolts to maintain confinement for operation above $6\,bars$.

The geometry of the filtration unit, illustrated in Figure 2, is typical[29] and was manufactured by Delft University of Technology. The inlet of the CFFU leads the fluid into a channel that soon assumes a constant rectangular cross-section $(25.4\,mm \times 4.0\,mm)$, where the flow profile develops fully before reaching the core face. The suspension can then flow through the core (permeate flow) or continue to flow along the channel and exit through the outlet adjacent to the inlet (crossflow).

The experiments presented in this article differ from typical crossflow experiments in several points:

1. the conducted experiments were flow rate controlled. The flow rate controller (manufactured by Nord Bargteheide) was set to a prescribed value, ensuring constant permeate and crossflow velocities within experimental error of $\sim 5\%$.
2. the crossflow channel was kept in a vertical rather than horizontal plane, so that the axial centreline of the cores was concentric with the CT scanner's centreline – see Figure 3.
3. the sandstone cores were drilled and sawn to a cylindrical geometry, instead of cuboid, to mitigate unwanted artefacts arising from the scanning and image reconstruction processes.

Bentheim sandstone was selected for these experiments for its quasi-homogeneous properties and low impurity content. Typical permeability is around $1.6D$, and pore throat diameter is in the range $10 - 15\mu m$. Quartz content exceeded 95%, with non-swelling clays making less than 2% of the sandstone. The cylindrical cores of $25.4\,mm$ diameter and $\sim 34\,mm$ length were placed concentrically inside a PVC shell, and glued in place using Araldite CW2215 with hardener HY5160 (manufactured by Rencast previously known as RenShape). After curing, the two ends of the core were sawn off. Accounting for the penetration of the glue into the core, the final effective dimensions of the core were $22\,mm$ in diameter and $20\,mm$ in length.

The injected water was comprised of distilled water (effectively $10^{-5}\,M$ of NaCl) containing hematite (Fe_2O_3) particles. A narrow-band particle size distribution was selected: $0.1\,\mu m - 5.0\,\mu m$ where 65% of the particles were less than $1.0\,\mu m$ in diameter.

Hematite was chosen for several reasons: its density $(5300\,kg/m^3)$ contrasts with that of water $(1000\,kg/m^3)$ and quartz $(2350\,kg/m^3)$, making it an ideal candidate for detection by the CT scanner; it is chemically distinguishable, as no iron atoms are natively present in Bentheim sandstone; and it is visually detectable, being red in colour while quartz is white.

Seven experiments, labelled **T2** through **T8**, were conducted with varying parameters: permeate rate, crossflow rate, and inlet suspension concentration – see Table 1. The CT scanner was set to acquire the data at the following specifications: voxel size = $(350 \times 350 \times 1000\mu m)$; energy = $80\,keV$; current = $250\,mA$; scanning mode = "spiral"; Somaris Syngo software filter = "B45 S medium"). The minimum voxel size allowed by the CT scanner was chosen, while the energy level was set to ensure the highest sensitivity to hematite deposition.

Each sweep or scan series took approximately $9\,sec$, and the time between scan series was set arbitrarily such that earlier series were closer to each other in time than later ones. At the end of each series, the effluent of the permeate flow was collected for chemical analysis. Each experiment was ended immediately after the last effluent sample was collected ($< 30\,sec$ from the last series). The sandstone core was then removed from the PEEK holder and dried in an oven at 70°C for 48 hours, after which it was scanned again to obtain the post mortem scan series. After removing the outer PVC shell the core was symmetrically split along the axial axis. One half was subjected to a final CT quantification, after which it was crushed and subjected to chemical analysis[21] to independently quantify the hematite content and establish a calibration. Due to the short length of the cores, a single value for the cumulative deposition $\int_0^1 \sigma(X)dX$ over each core was obtained. The other half was cured in epoxy, had thin sections produced and was subjected to scanning electron microscopy (SEM). Details of the data processing are provided in the following section.

5 Data acquisition and processing

Three distinct regions where data was collected can be defined: the influent area $(R1)$; the core segment $(R2)$; and the effluent area $(R3)$. The data acquired in each region will be described. Details of the pre-modelling treatment of the data will also be described in this section. First, however, a general description of the data generated by the SAMATOM CT scanner will be given.

5.1 Description of CT scanner data

The CT scanner was set to sweep the setup in the direction of the injection starting at a point just before the core starts and ending just after the wide orifice area of the PVC dummy, as illustrated in Figure 4. This spatial frame, over which the sweeps were made, was maintained throughout each experiment. Each sweep was manually triggered by the CT scanner operator and produced a series of 2-dimensional images – an example of which is given in Figure 17.

These images were processed and compiled from the measurements of multiple detectors by the CT scanner's accompanying software, Somaris Syngo. The images were stored in the medical industry DICOM standard and are 12-bit indexed; i.e. 4096 levels ranging from -1024 to $+3071$. The pixel values are the computed linear attenuations μ normalised to CT numbers n_{CT} in Hounsfield[30] Units (HU), by

$$n_{CT} = 1000 \cdot \left(\frac{\mu - \mu_w}{\mu_w} \right). \qquad (9)$$

Here μ and μ_w are the linear attenuation coefficients of the object under investigation and pure water respectively. Thus, the CT number of a pixel is proportional to the X-ray attenuation in the corresponding voxel's content relative to the X-ray attenuation in water[28]. It follows from (9) that the CT number of water is $0HU$ and around $-1000HU$ for air, which has a linear attenuation coefficient of around zero.

The DICOM images were processed using MATLAB[31] scripts developed by the authors. The different image slices constituting a series were tagged according to which of the three regions they belonged to, in order to automate processing. Image stencils were then used to crop the relevant portions of each image. Figure 4 illustrates the various stages of image processing for the core region $R2$. The final cropped area from each slice image was used to obtain an average CT value, and the associated standard deviation.

5.2 Data acquisition over the influent and effluent concentration regions

The $4\,mm$ thick crossflow channel comprised the influent area $(R1)$. A stainless steel needle pressure tap located at the core face was used, in conjunction with the inlet reference pressure gauge, to measure the pressure drop over any developing filter cake – see differential pressure gauge $dp1$ in Figure 1. A pressure buildup of $\sim 10\,mbar$ was measured in experiments **T4** and **T6**, while a $75\,mbar$ pressure buildup was detected in **T8**. Unfortunately, no pressure drop was detected over $dp1$ in the other four experiments.

Calibration tests using hematite suspensions of known values in polyethylene bottles were conducted. The absence of the PEEK setup and supporting aluminium bolts yields lower noise and better quality data. The calibration experiments at the previously mentioned CT scanner settings indicated that any suspension concentration below a detection threshold $\tilde{c}_{th}$ of $400\frac{mg}{L}$ $(75.5\,ppm)$ would be masked by noise – see Figure 5. The maximum injected suspension concentration, which was $60\frac{mg}{L}\,(12\,ppm)$ in experiments **T6** through **T8**, falls short of the threshold value $\tilde{c}_{th}$. Thus, one does not expect it to be possible to measure the influent and effluent concentration using the CT scanner. Still, the developed external filter cake, which was visually observed at the end of the experiment (Figure 6), should have been detectable. The fact that no valuable CT data was extracted from $R1$ is attributed to the presence of the stainless steel pressure tap that had a severe negative impact on the quality of the data.

The effluent region $(R3)$ comprised the large orifice area of the PVC dummy following the core – see Figure 2 and slices 6C-8B of Figure 17. A stencil was used to crop the image to the effluent portion of the image only. The measurements obtained were unusable as predicted by the calibration tests. Effluent samples were also collected further downstream of the scanned region for chemical analysis – see Figure 7.

5.3 Data acquisition over the core region

Two differential pressure gauges were placed across the core: $dp2$ straddled the core inlet face and a point $7\,mm$ along the core length corresponding to $X = 0.35$. A second differential pressure gauge $dp3$ straddled the $7\,mm$ point and a point subsequent to the core outlet face. Since the pressure drop in the dummy and tubings after the core is negligible, this point is considered $X = 1.0$. Furthermore absolute pressure gauges $p1$ and $p2$, corresponding to the backpressure and pump head pressure, were used to gauge the pressure drop over the core and cake. Figure 8 illustrates the impedance curves of some of the conducted experiments.

The Bentheim cores used in these experiments were $20.0\,mm \pm 0.2\,mm$ long. Thus, theoretically 20 CT slices should be available for analysis from each scan series. Following the cropping technique mentioned previously, average CT values and their standard deviations were extracted for each cropped element corresponding to $1.0\,mm$ slices of the core. Comparison between identical slices from different scan series allows for the description of the deposition profile evolution in time. A base scan series was conducted at the prerequisite experimental conditions prior to switching the injection fluid from distilled water to hematite suspension. Thus, any increase in the measured average CT number in subsequent scan series can be attributed to the deposited hematite – see Figure 9. The relative average CT number profile $\bar{\sigma}(X,T)$ is defined as the difference between subsequent series $n_{CT}(X,T>0)$ and the base series $n_{CT}(X,0)$.

It should be noted that although 20 slices per series could be obtained under ideal conditions, this was not the case in these experiments. One of the two aluminium flanges used to maintain seal conditions under high pressure, visible in slices 5C-6E of Figure 17, overlapped the last $5\,mm$ of the core. The extracted average CT numbers from the scans corresponding to and adjacent to the overlap region were rendered useless due to the unacceptable high noise to signal ratio. Similarly, the stainless steel pressure tap at the inlet face of the core rendered the first slice unusable. Thus, the number of slices that could be used for analysis varied from $11-15$ depending on the experiment – see Figure 9. This made it difficult to correlate the relative CT numbers $\bar{\sigma}(X,T)$ to the deposition profiles $\tilde{\sigma}(X,T)$, as is explained below.

5.4 Core region data processing

Deposition profiles can be correlated to CT numbers using two main techniques. One technique is using theoretical models available in the literature, while the other is the matching of the chemically quantified deposition profile to its corresponding final CT scan deposition profile. Theoretical models could not account for the effect of the surrounding setup. The online scan series $n_{CT}(X,T)$ are truncated measurements with approximately $\sim 35\%$ of the data missing. The post mortem series suffered from end effects and had a loss of $\sim 5\%$. The lack of a pre-experiment scan series at conditions identical to the post mortem series makes it impossible to correlate the data without some extrapolation.

It should be noted that the voxel has a length of $1000\,\mu m$, and the core faces may not necessarily start or end at precise voxel boundaries. The left and right boundaries of usable data (x_a and x_b) coincide with voxel boundaries. For most experiments, x_a is less than $1.0\,mm$ away from the injection face. On the other hand x_b is on average $6.0\,mm$ away from the effluent face due to the noise caused by the aluminium flange as described previously. The dimensionless coordinate X is defined using (5) relative to the core injection face.

Time was nondimensionalised into PVI using

$$T = \frac{1}{L\phi} u_p (t - t_{switch} - \frac{V}{Q}) . \quad (10)$$

where t is the time passed since the experiment started with clean water injection, and t_{switch} is the time passed until the feed tanks were switched from clean water to suspension. V is the volume between the feed tanks and the core face, while Q is the injection rate of the experiment comprising both permeate and crossflow rates.

The average time taken to scan a slice is $250\,ms$ so that scanning over the range $[X_a, X_b]$ takes at most $4\,sec$. The time taken to inject one pore volume varied between $0.85\,sec$ and $1.75\,sec$ depending on the experiment injection conditions, while scan series were set apart by a minimum of $170\,sec$. Therefore, the error introduced by assigning a single timestamp to each scan is negligible.

6 Parameter optimisation

The model for deep-bed filtration described previously will now be adjusted to the data. The procedure comes down to finding the best parameterisations for the filtration function $\lambda(\sigma)$ and the effective injected concentration. These parameterisations should yield the best approximation to the experimental data as a solution to equations (6) and (7). The following subsection presents the optimality criteria adopted and the methodology employed to achieve it. Next, analysis of model-consistent behaviour at the injection face is performed. Finally, the mathematical tools developed herein are used to find a correlation between the CT scanner data and the chemical analysis of the core.

6.1 Profile fitting

The reference experimental values to which the model is to be adjusted are the $\overline{\sigma}_j(X, T_j)$ profiles, defined as constant in each segment of a uniform partition of the $[X_a, X_b]$ interval. Since in the model the profiles are smooth curves, the first step is to approximate these discontinuous data by cubic splines. The optimal set of splines was obtained minimizing the cost function

$$C(\sigma) = \sum_j \left(\int_{X_a}^{X_b} \overline{\sigma}_j dX - \int_{X_a}^{X_b} \sigma_j dX \right)^2 \quad (11)$$
$$j = 1,\ldots,N_{scan}$$

where the first integral is just the sum of $\overline{\sigma}$ for a particular scan, and the second is the integral of the cubic spline used to approximate it. A first guess was easily obtained by linearly interpolating and extrapolating the values defined over the segments to their boundary nodes.

The profiles thus obtained are smooth, and their numerical differentiation provides enough data to find an average value of $\lambda(\sigma)$ to be used as a first guess in the optimisation procedure. The optimal values for each of the three parameterisations were obtained minimizing the cost function

$$C(\hat{\sigma}) = \sum_{i,j} \left(\int_{X_i}^{X_{i+1}} \hat{\sigma}_j dX - \int_{X_i}^{X_{i+1}} \overline{\sigma}_j dX \right)^2 \quad (12)$$
$$i = 1,\ldots,N, j = 1,\ldots,N_{scan}$$

where $\hat{\sigma}$ is the solution of equation (7) over the $[X_a, X_b]$ interval, using some point of the previously obtained splines as starting point.

Not all scans were used in these minimizations: the earlier were truncated or completely discarded because their values were of the same order as the noise they contained.

6.2 Inlet deposition

Integrating equation (7) all the way back to $X = 0$ yields N_{scan} values $\sigma(0, T_j)$, that should correspond to the solution of equation (6) using initial value $\sigma(0,0) = 0$ and the yet to be determined $c_i(T)$ function. The shape of the latter was first assumed to be constant per segment. Using the available data points, the integral

$$\int_{\sigma_j}^{\sigma_{j+1}} e^{\alpha\sigma} d\sigma = \overline{c}_i \lambda_0 \int_{T_j}^{T_{j+1}} dT$$

derived from (6) and (8) was solved and yields

$$\overline{c}_i(T_j) = \frac{e^{\alpha(\sigma_j - \sigma_{j-1})} - 1}{\lambda_0 \alpha (T_j - T_{j-1})}$$
$$j = 1,\ldots,N_{scan} \quad (13)$$
$$T_0 = \sigma_0 = 0$$

for the exponential filtration coefficient. Similarly, simpler integrals were derived and solved for the other two cases. The stair functions obtained from these indicate $c_i(T)$ to be an exponentially decreasing function of time converging to a positive asymptote. The effective injection concentration is therefore parameterised as $c_i(T) = \alpha e^{\beta T} + \gamma$, and its parameters are optimised together with those of $\lambda(\sigma)$ using again the cost function (12). This may appear to be redundant, but has considerable effect on all parameters, since now the $\hat{\sigma}$ profiles are the solution of equations (6) and (7) using $\sigma(0,0) = 0$ as starting point. Figure 11 shows the best fit obtained through this process.

6.3 Calibration of CT Data to Chemical Analysis

There are three post mortem scans for each experiment: the first two are redundant, and the third was done after shifting the core by $1.5\,mm$ in the scanner frame. All the interference the online scans had is missing now, so useful data can be recovered for all the core length, except its extremities. The X interval was determined and mapped using the same method and algorithms as for the online scans. Once properly aligned, the values of the three post mortem scans were averaged into a single profile.

The post mortem average profiles were lower than their corresponding final online profiles by $\sim 170\,HU$. This is attributed to the presence of water in the core in the online scans, which was replaced by air in the post mortem scans. Assuming that the removal of the water and the injection setup has a linear homogeneous effect over the matchable sections of the core, one would expect this difference to be proportional to the porosity ($\phi \approx 22\%$, corresponding to $220\,HU$).

The values used in our previous analyses were the difference between the first online scan and each following one. The post mortem profiles were vertically shifted, subtracting from them the averages of the post mortem and first online scans over the $[X_a, X_b]$, and adding the average of the last online scan. As expected, low readings in the $[X_b, 1]$ interval went

inside the noise level range, and we restricted the data to non-negative values only.

Finally, to obtain the proportionality factor between CT values and hematite deposition concentration, that is

$$\frac{\phi L A \int_0^1 \sigma dX}{\text{mass}_{Fe_2O_3}}$$

where L is the core length and A the cross section area, first the injection end of the post mortem profile is completed using the same method as before – see §6.2. The profiles vanish before $X = 1$ for all cases. Figure 12 shows the comparison of the known suspension concentration and the effective injection concentration, as recovered in the previous section and scaled in this one.

7 Conclusions and Recommendations

The results obtained from the CT scanner are novel and of great value. The attained average CT number profiles were satisfactorily correlated to deposition profiles within the core above a threshold value of $400\frac{mg}{L}$, which corresponds to 0.035% of the porosity of the Bentheim cores used. Despite design flaws, namely the use of aluminium and PVC in the setup that truncated the useful data, modelling and recovery were successful.

The model applied was based on the classical deep-bed filtration model. The method of characteristics was used to solve the equivalent system of linear ODEs. Experimental data used in the modelling comprised the deposition profiles $\overline{\sigma}(X,T)$ for several values of T and known value of effective inlet concentration when the experiment started $c_i(0)$. Solution by optimisation over the domain of useful data allowed the extraction of the optimal parameters of the three proposed filtration functions defined by (8). The exponential form of the filtration function yielded a somewhat better match than either the linear form or the constant form. Figure 11 presents the properly scaled deposition profiles, as recovered from the online scans and reproduced by the model for experiment **T3**. Figure 12 illustrates the comparison between the specified injected suspension concentration and the hypothetical exponentially decreasing curve of effective injected concentration, as required for the model to be consistent. The effluent concentration curves generated by the model and the experimental measurements are presented in Figure 7. Experiments **T2** through **T5** yielded similar plots. Experiments **T6** through **T8** where not fully analysed at the time of this publication.

The validity of the model can be further verified as follows. Equations (1) and (2) of the CDBFM yield the ODE over characteristics – equation (7). It follows that adding a constant to X in the dX term will not affect the validity of the equation. Thus, each of the different deposition profiles $\overline{\sigma}(X,T)$ can be shifted along X to yield a single continuous deposition curve, which would originate from the same filtration function in a longer virtual core. If a match is not obtained then the model defined by equations (1) and (2) comes into question. The phenomenological kinetics equation (2) is more likely of being the culprit of any discrepancy than the continuity equation (1). The results of shifting the earlier CT number profiles of experiment **T3** by the same dX as the model solution is illustrated in Figure 16. It can be seen that a reasonable fit is obtained. However, the discrepancy observed at the tails of each profile indicates that the model is not exact, and that measuring the deposition profiles by a CT scanner has the potential of quantifying the proper model's correction.

For all analysed experiments, at time zero, the injected concentration consistent with the model is comparable to the suspension value – see Figure 7. This indicates that the CDBFM is reasonably consistent with the measured phenomena, pointing towards cake formation as the most important issue to be addressed next. The dynamics of cake formation are required to validate the decreasing values obtained for the actually injected concentration. The filtration across the four first experiments is not as invariant as would be expected, showing sensitivity to crossflow and permeate velocities that point to cake formation, given that the same type of porous rock was used in all tests and that the coefficient should be a property of the rock and particles alone. Figure 15 shows the different $\lambda(\sigma)$ recovered.

The effluent concentration of the permeate flow was collected and analysed chemically – see Figure 7. The prediction of the effluent profile from the forward solution of the model based on the parameters attained for all three variations of filtration function (8) yields a monotonically declining effluent profile after the breakthrough. Thus, not only is the scale of the predicted profile inconsistent with the experimental measurements, but so is the shape. However, the extrapolation of the deposition profile tails could account for this discrepancy.

It can therefore be concluded that the CDBFM is valid as an approximation. It also brings into question analyses based on effluent concentration measurements, confirming mathematical analyses[18] that show that recovering CDBFM parameters from the effluent concentration is an ill-posed problem. Assuming equal trustworthiness of deposition data and effluent data, it becomes evident that the more stable problem posed by using the deposition profiles is more favourable.

Analysis of the measured pressure drops and associated impedance curves has not been conducted. Yet, superficial observation of the impedance profiles (Figure 8) illustrates that deposition or its impact on permeability is consistent with cake formation since early times[18]. Therefore, the validity of either the currently and previously[16] presented experiments or the phenomenological kinetics equation is brought into question.

Improvements to the setup are required to reduce the noise in obtained data, allowing for more affirmative conclusions on the kinetics equation (2). These modifications include redesigning the setup to increase its pressure confinement from $12\,bar$ to $35\,bar$, while eliminating the use of any non-PEEK materials. This will allow for the use of longer cores up to $\sim 50\,mm$ as well as for minimisation of data truncation. Maintaining a constant radial cross section along the entire setup will help in minimising the variability of X-ray energy attenuation outside the zone of interest. Furthermore, a technique for independently measuring or maintaining the effective inlet concentration is required. Alternative methods of quantifying the effluent concentration at a higher temporal resolution are required. Quantification of the crossflow effluent concentration is necessary to quantify the amount of particles forming the external filter cake.

Furthermore, the assumption that hematite deposition has a linear effect on the CT number needs to be verified experimentally. The core region of the setup ($R2$) should be filled with homogeneous mixtures of sand and known concentrations of hematite. Scans of the mixture when both dry and fully saturated with water should be made to establish a calibration curve for hematite deposition inside a quartz based porous medium (Betheim sandstone) as was done for the suspension in §5.2.

A new setup has been designed and built to meet the design criteria mentioned above. Enhancements to the measurement techniques are currently being investigated.

8 Nomenclature

$\tilde{c}$ *solid particle concentration in suspension;* $[ppm]$
c *normalised solid particle concentration in suspension* $= \tilde{c}/\tilde{c}_0$ *;* $[-]$
c_i *injected hematite suspension concentration;* $[ppm]$
n_{CT} *CT number;* $[HU]$
t *time;* $[sec]$
u_p *superficial (Darcy) permeate velocity;* $[m \cdot sec^{-1}]$
x *coordinate along core's centreline in injection direction;* $[m]$
D *hydrodynamic dispersion coefficient;* $[m^2 \cdot sec^{-1}]$
L *length of the core;* $[m]$
Q *flux of particles;* $[m \cdot sec^{-1}]$
T *dimensionless time coordinate in* $[PVI]$
X *dimensionless spatial coordinate;* $[-]$
ϕ *porosity;* $[-]$
λ *filtration function* $[m^{-1}]$
μ *Linear attenuation coefficient* $[cm^{-1}]$
σ *deposited solid particles concentration;* $[ppm]$
$\tilde{\sigma}$ *normalised deposition profile* $= \sigma/c_0\phi$ *;* $[-]$
$\bar{\sigma}$ *relative average CT numbers;* $[HU]$

9 Acknowledgements

The authors would like to acknowledge their supervisors (Peter K. Currie, Dan Marchesin, Wim M.G.T. van den Broek and Pacelli Zitha) for their contribution and support without which this work would not have been possible. The technical staff at the Dietz Laboratory (Leo Vogt, Adri Maljaars and Andre Hoving) are thanked. Sponsorship from PDO, Shell, NWO and NIOC is acknowledged. The experiments were conducted using the X-ray computer tomography machine provided by the Dutch Technology Foundation (STW) through project DAR.5756.

10 References

1. Simpson, A.J. and R.W. Paige. Advances in Forties Field Water Injection. in Offshore Europe Conference. 1991. Aberdeen: SPE 23140.
2. Parker, D.H., C.A.T. Kuijvenhoven, R.D. Waterland, and M. Smies. Oil Production and Water Management in Oman. in First International Conference on Health, Safety and Environment. 1991. The Hague, The Netherlands: SPE 23322.
3. King, R.E. Maureen Produced Water Injection. in Offshore European Conference. 1993. Aberdeen, U.K.: SPE 26703.
4. Khatib, Z. and P. Verbeek. Water to Value - Produced Water Management for Sustainable Field Development of Mature and Green Fields. in SPE International Conference on Health, Safety and Environment in Oil and Gas Exploration and Production. 2002. Kuala Lumpur, Malaysia: SPE 73853.
5. Evans, R.C. Developments in Environmental Protection Related to Produced Water Treatments and Disposal (Produced Water Re-Injection). in Second International Conference on Health, Safety & Environment in Oil & Gas Exploration & Production. 1994. Jakarat, Indonesia: SPE 27179.
6. Allen, R.M. and K. Robinson. Environmental Aspects of Produced Water Disposal. in SPE Middle East Oil Technical Conference & Exhibition. 1993. Bahrain: SPE 25549.
7. Evans, P. and K. Robinson. Produced Water Management - Reservoir and Facilities Engineering Aspects. in 1999 SPE Middle East Oil Show. 1999. Bahrain: SPE 53254.
8. Iwasaki, T., Some notes on sand filtration. Journal of the American Water Works Association, 1937. 29: p. 1591-1602.
9. Herzig, J.P., D.M. Leclerc, and P. Le Goff, Flow of suspensions through porous media - application to deep filtration. Industrial and Engineering Chemistry, 1970. 65(5): p. 8-35.
10. McDowell-Boyer, L.M., J.R. Hunt, and N. Sitar, Particle transport through porous media. Water Resources Research, 1986. 22(13): p. 1901-1921.
11. Saripalli, K.P., M.M. Sharma, and S.L. Bryant, Modeling injection well performance during deep-well injection of liquid wastes. Journal of Hydrology, 2000. 227: p. 41-55.
12. Bedrikovetsky, P., D. Marchesin, G. Hime, A. Alvarez, A.O. Marchesin, A.G. Siqueira, A.L.S. Souza, F.S. Shecaira, and J.R. Rodrigues. Porous Media Deposition Damage from Injection of Water with Particles. in VIII ECMOR. 2002.
13. Bedrikovetsky, P., D. Marchesin, G. Hime, A.G. Siqueira, A.L. Serra, and J.R. Rodrigues. Inverse Problems for Treatment of Laboratory Data on Injectivity Impairment. in. 2004. SPE 86523.
14. Alvarez, A.C., P. Bedrikovedsky, G. Hime, D. Marchesin, and J.R. Rodrigues, A fast inverse solver for the filtration function for flow of water with particles in porous media, submitted to Inverse Problems in 2005
15. Bedrikovetsky, P., D. Marchesin, F.S. Shecaira, A.L.S. Souza, P. Milanez, and E. Rezende, Characterisation of Deep-Bed Filtration System from Laboratory Pressure Drop Measurements. Journal of Petroleum Science and Engineering, 2001. 64(3): p. 167-177.
16. Al-Abduwani, F.A.H., B.-R. de Zwart, R. Farajzadeh, W.M.G.T. van den Broek, and P.K. Currie. Utilising Static Filtration Experiments to Test Existing Filtration Theories for Conformance. in 2nd Produced Water Workshop. 2004. Aberdeen, United Kingdom: NEL.
17. Alvarez, A., G. Hime, D. Marchesin, and P. Bedrikovedsky, The inverse problem of determining filtration function and permeability reduction in porous media, submitted to in 2005
18. Alvarez, A.C., Inverse problems for deep bed filtration in porous media, in Department of Fluid Dynamics. 2004, IMPA - Instituto Nacional de Matemática Pura e Aplicada: Rio de Janeiro. p. 149.
19. Marchesin, D., A.C. Alvarez, G. Hime, P. Bedrikovedsky, and F.A.H. Al-Abduwani. The inverse problem of determining filtration function and permeability reduction in porous media. in XXV CILAMCE. Iberian Latin American Congress on Computational Methods. 2004. Recife, Brazil.
20. Kau, S. and F.D. Lawler, Dynamics of Deep-Bed Filtration: Velocity, Depth and Media. Journal of Environmental Engineering, 1995. 121(12): p. 850-859.
21. Al-Abduwani, F.A.H., A. Shirzadi, W.M.G.T. van den Broek, and P.K. Currie. Formation Damage vs. Solid Particles Deposition Profile during Laboratory Simulated PWRI. in SPE European Formation Damage Conference. 2003. The Hague, The Netherlands: SPE 82235.

22. Al-Abduwani, F.A.H., R. Farajzadeh, W.M.G.T. van den Broek, P.K. Currie, and P.L.J. Zitha, Filtration of Micron-Sized Particles in Granular Media Revealed by X-ray Computed Tomopraphy, submitted to Review of Scientific Instruments in 2004
23. Elimelech, M., J. Gregory, X. Jia, and R.A. Williams, Particle Deposition & Aggregation: Measurement, Modelling and Simulation. Paperback ed. Colloid and Surface Engineering, ed. R.A. Williams. 1998, Woburn: Butterworth-Heinemann. 441.
24. Logan, J.D., Transport Modeling in Hydrogeochemical Systems. 2001: Springer.
25. Bai, R. and C. Tien, Effect of Deposition in Deep-Bed Filtration: Determination and Search of Rate Parameters. Journal of Colloid and Interface Science, 2000. 231: p. 299-311.
26. Song, L. and M. Elimelech, Theory of Concentration Polarization in Crossflow Filtration. Journal of the Chemical Society, Faraday Transactions, 1995. 91(19): p. 3389-3398.
27. Al-Abduwani, F.A.H., P. Bedrikovedsky, R. Farajzadeh, W.M.G.T. van den Broek, and P.K. Currie. External Filter Cake Erosion: Mathematical Model and Experimental Study. in SPE 6th European Formation Damage Conference. 2005. Scheveningen, The Netherlands: SPE 94635.
28. Kalender, W.A., Computed Tomography: Fundamentals, System Technology, Image Quality, Appications. 2000, Munich: Publicis MCD Verlag. 220.
29. Jiao, D. and M.M. Sharma, Mechanism of Cake Buildup in Crossflow Filtration of Colloidal Suspensions. Journal of Colloid and Interface Science, 1994. 162: p. 454-462.
30. Hounsfield, G.N., Godfrey N. Hounsfield - Autobiography. Published by Nobelprize.org at (http://nobelprize.org/medicine/laureates/1979/hounsfield-autobio.html). Accessed in 2005
31. The MathWorks, Natick, Massachusetts, U.S.A, (www.mathworks.com).

11 Tables

Table 1: Parameters of the conducted experiments

	$Q[L/hr]$	$u_p\,[10^{-3}m/s]$	$\tilde{c}_0\,[mg/L]$	$u_{cf}\,[10^{-3}m/s]$
2T	10.4	3.66	27.08951	14.6
3T	8.6	4.05	27.08951	8.36
4T	10.1	5.15	30.52936	8.47
5T	11.1	5.15	37.09262	11.1
6T	7.6	2.67	59.90861	10.7
7T	8.3	2.22	61.16302	14.3
8T	6.1	2.94	63.21278	5.66

12 Figures

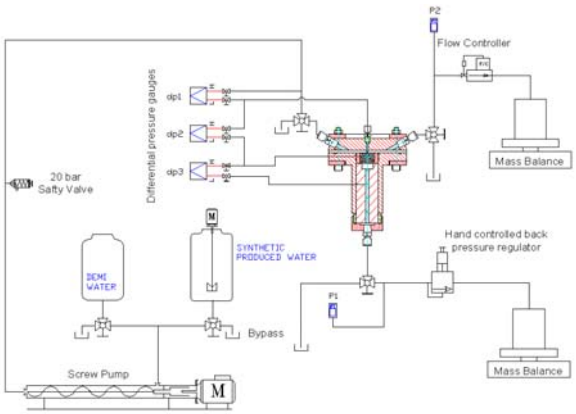

Figure 1: Schematic of the crossflow filtration setup depicting the crossflow filtration unit (CFFU), injection unit (IU) and effluent concentration detection unit (ECDU).

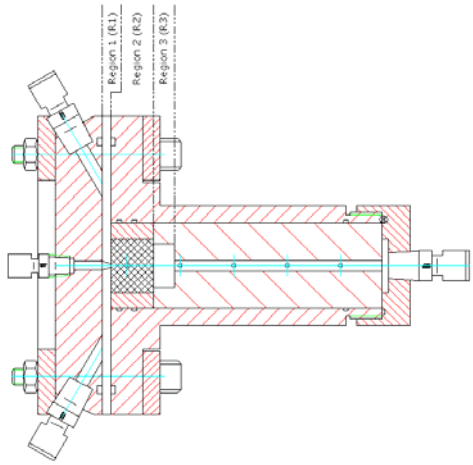

Figure 2: Schematic of the crossflow filtration unit

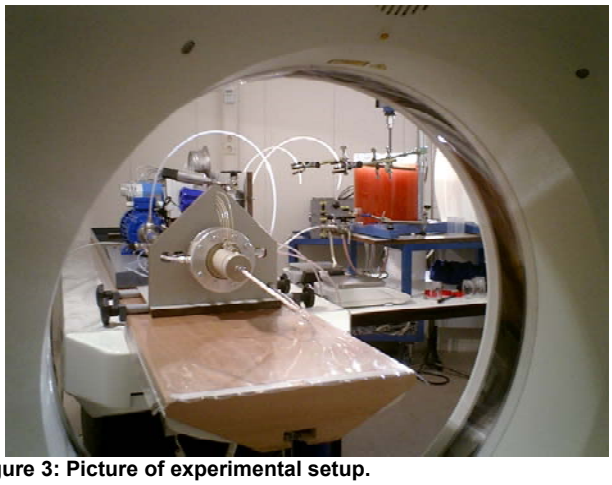

Figure 3: Picture of experimental setup.

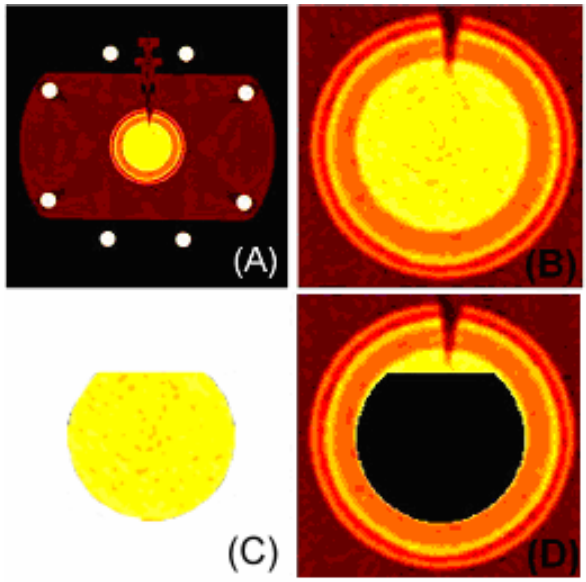

Figure 4: Example of CT slice image processing stages: (a) the raw 512x512 image obtained from the core region (R2), (b) a rectangle containing the area of interest, (c) the cropped area of interest, as determined by visual analysis, (d) the surrounding discarded data.

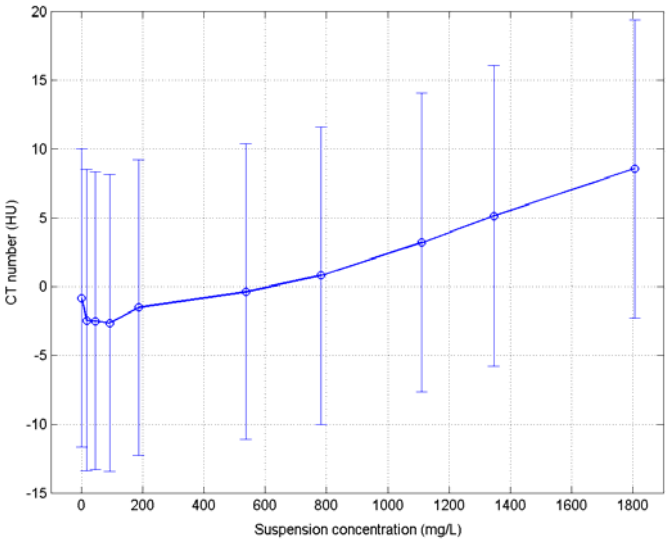

Figure 5: Average CT values of the different calibration suspensions.

Figure 6: Example of observed filter cakes at the end of an experiment.

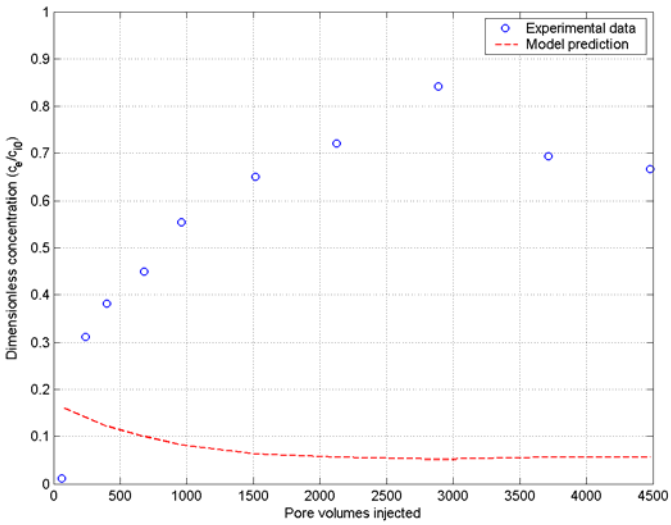

Figure 7: Effluent concentration measurements of experiment T3 as quantified by chemical analysis (circle markers) and profile predicted by model (dashed line).

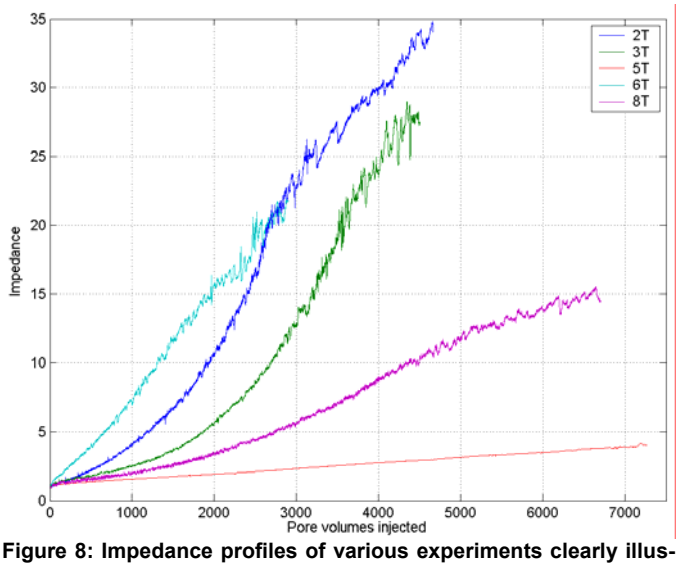

Figure 8: Impedance profiles of various experiments clearly illustrate different kinds of behaviour.

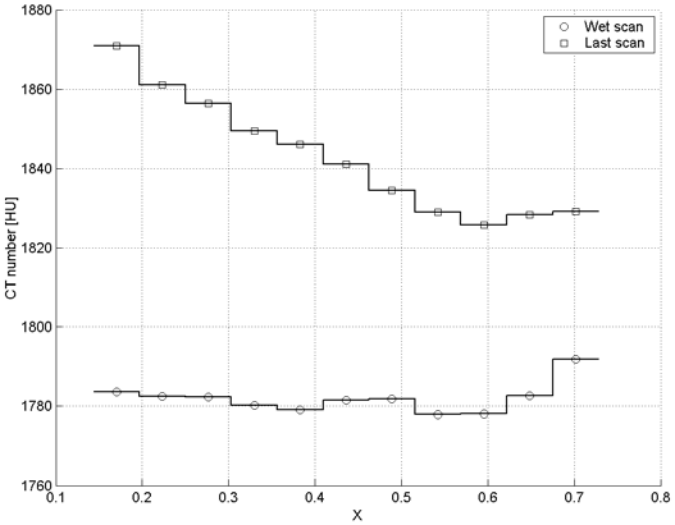

Figure 9: Deposition profile recovery: averaged CT values obtained for the base and last scan series of the core region (R2) in experiment T3.

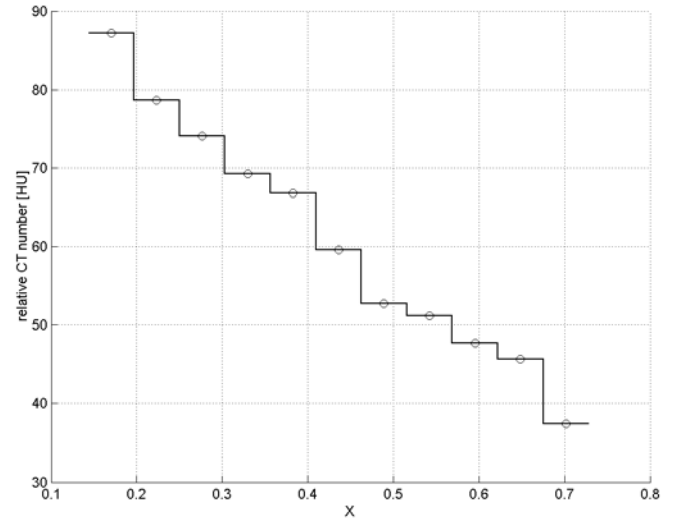

Figure 10: Difference between the last series and base series which is directly proportional to hematite deposition.

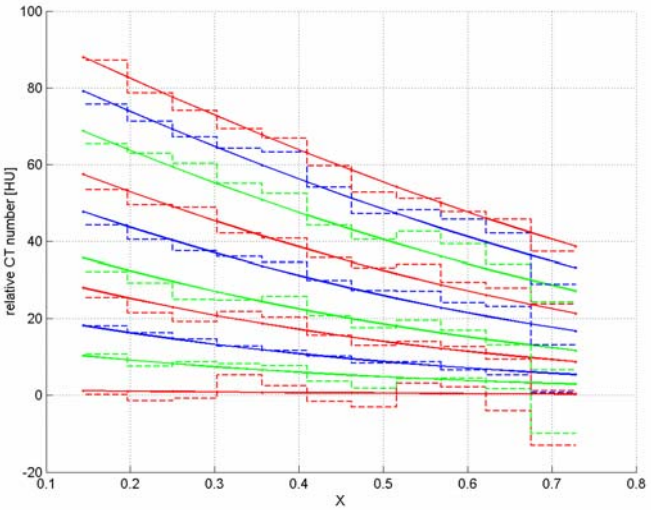

Figure 11: In dashed lines, the experimental data; in solid lines, the profiles generated by the model using the optimal exponential $\lambda(\sigma)$ parameters recovered in section 6.

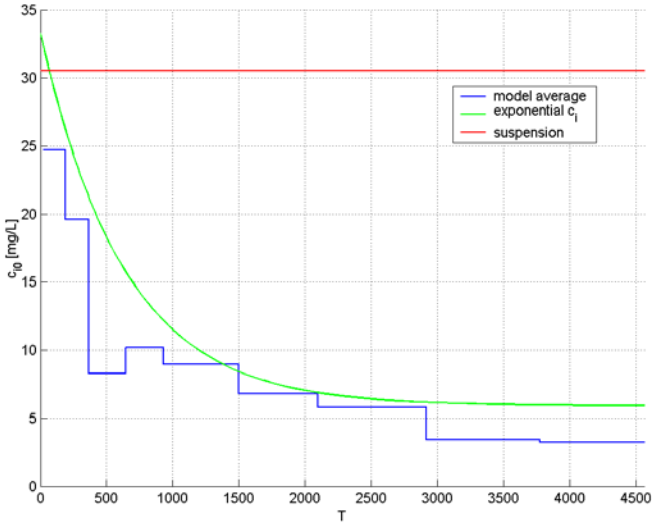

Figure 12: Time dependent injected concentration: the stair function is the approximation obtained solving equation (13), and the smooth curve is the optimal fit of the parameterisation relative to functional (12).

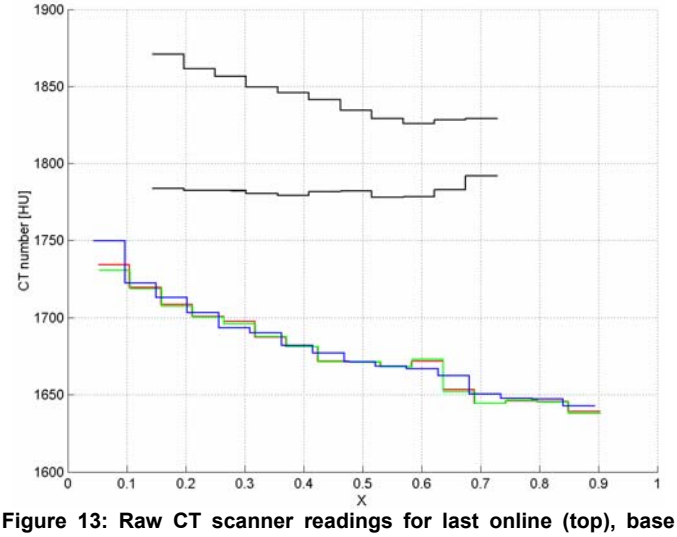

Figure 13: Raw CT scanner readings for last online (top), base (middle) and each post mortem scan (bottom). Data is horizontally matched for all scans.

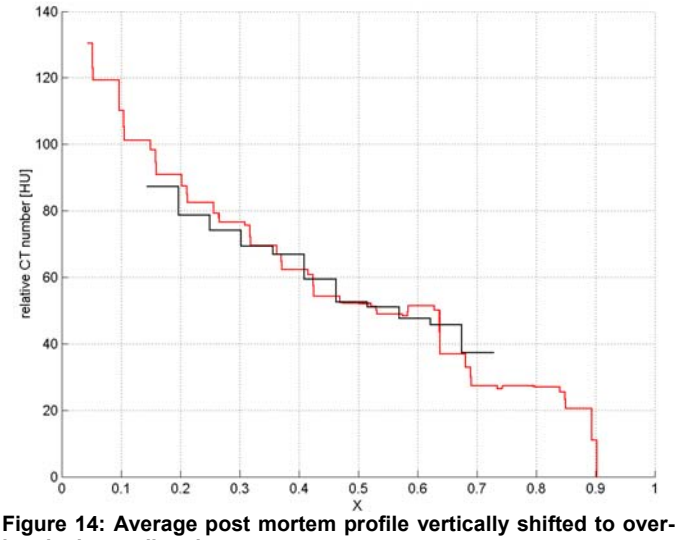

Figure 14: Average post mortem profile vertically shifted to overlap the last online data.

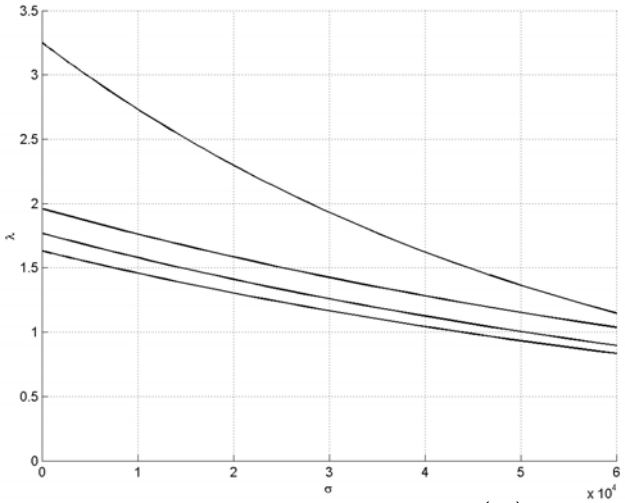

Figure 15: Comparison of optimal exponential $\lambda(\sigma)$ for the first four experiments: from top to bottom, the curves correspond to experiments T2 through T5.

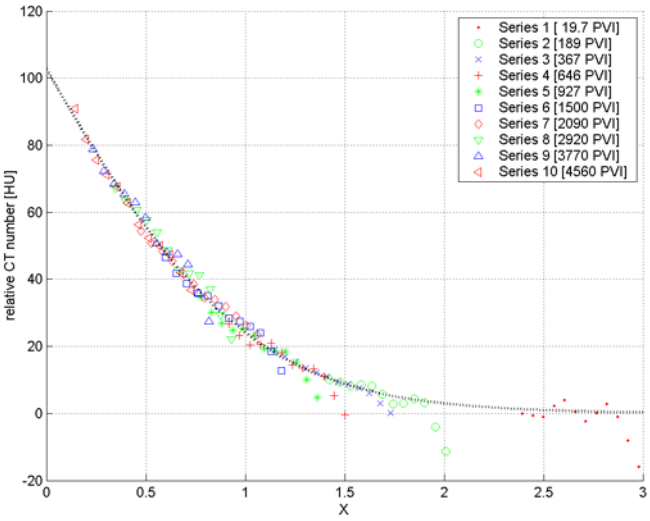

Figure 16: Global deposition profile obtained by the superimposition of the different deposition profiles of experiment T3.

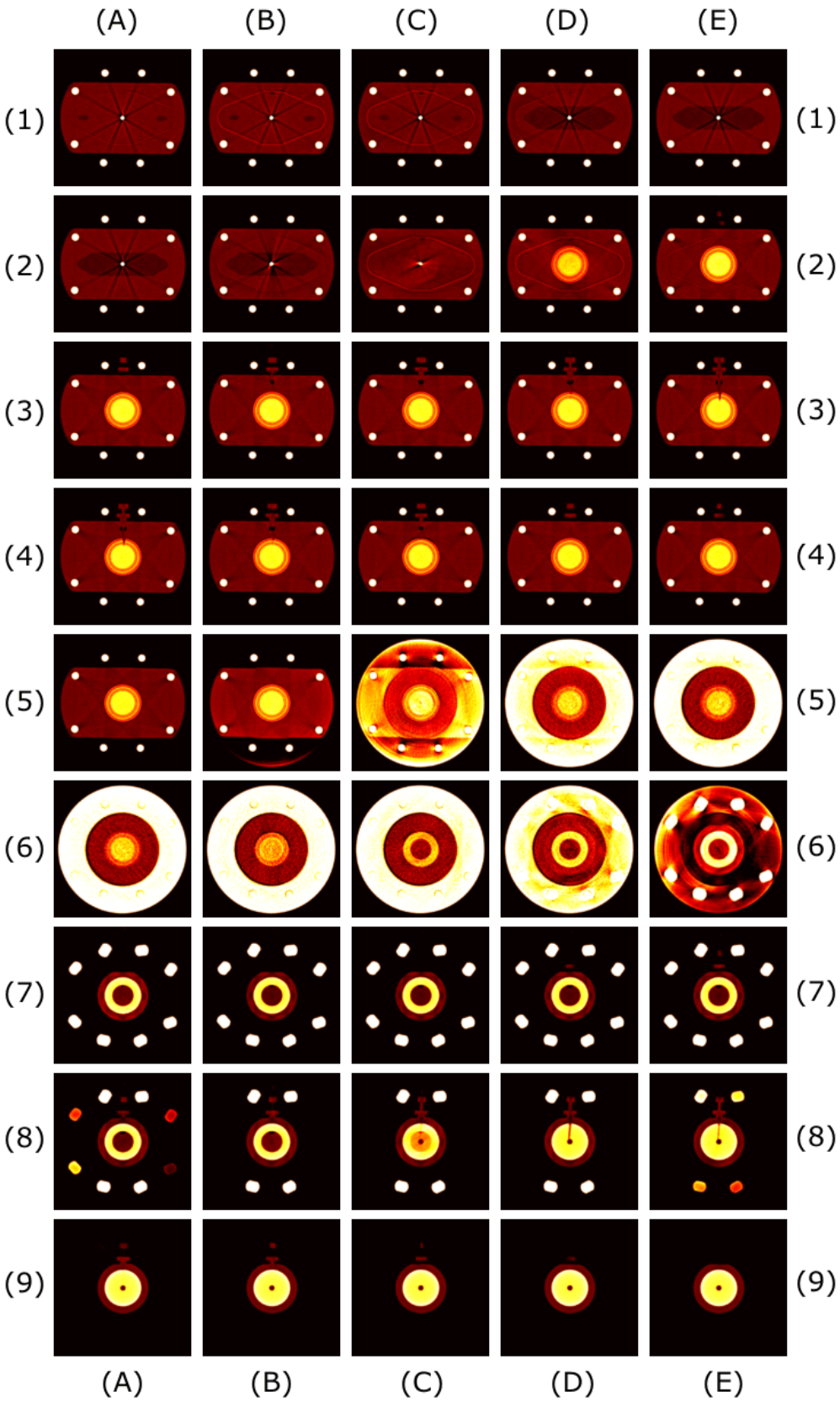

Figure 17: Slices from the base scan of T3, which was conducted prior to the injection of hematite suspension. Sequence of Images from left to right, top to bottom.